Effect of Ti addition on thermal stability and phase evolution of super-invar based yttria added ODS alloys developed by mechanical alloying and spark plasma sintering

Arpan Arora, Suhrit Mula

PII: S0925-8388(21)04746-0

DOI: https://doi.org/10.1016/j.jallcom.2021.163336

Reference: JALCOM163336

To appear in: *Journal of Alloys and Compounds*

Received date: 8 November 2021
Revised date: 15 December 2021
Accepted date: 18 December 2021

Please cite this article as: Arpan Arora and Suhrit Mula, Effect of Ti addition on thermal stability and phase evolution of super-invar based yttria added ODS alloys developed by mechanical alloying and spark plasma sintering, *Journal of Alloys and Compounds,* (2021) doi:https://doi.org/10.1016/j.jallcom.2021.163336

Effect of Ti addition on thermal stability and phase evolution of super-invar based yttria added ODS alloys developed by mechanical alloying and spark plasma sintering

Arpan Arora, Suhrit Mula*

Department of Metallurgical and Materials Engineering, IIT Roorkee, Roorkee 247667, India

*Corresponding Author: e-mail: suhrit.mula@mt.iitr.ac.in; suhritmula@gmail.com

Phone: +91-1332-285763; Fax: +91-1332-28524

Abstract

In the present study, Ti and Y_2O_3 nano-powders were introduced in a base composition of Fe-42wt.% Ni invar alloy to investigate their effects on phase evolution and its thermal stability. Three compositions, namely, Fe-42Ni-2Y_2O_3-0.3Ti, Fe-42Ni-2Y_2O_3-1Ti, Fe-42Ni-2Y_2O_3-2Ti (all in wt.%), were mechanically alloyed through high energy SPEX8000M ball mill with a varying amount of Ti (0.3, 1, and 2 wt.%). The milled compositions were consolidated by spark plasma sintering at 1000 °C at 60 MPa pressure with a holding time of 5 min. The addition of Ti and Y_2O_3 nano-powders in the Fe-Ni metal matrix is expected to develop nanoclusters precipitates, thereby increasing its strength by Orowan strengthening. Consequently, submicron size grain was found to form in the case of 2 wt.% Ti alloy (205 nm) as compared to 348 nm size grains in 0.3 wt.% Ti alloy. The corresponding composition dictated higher nanoindentation hardness values (4.4 GPa and 5.2 GPa, respectively), which also validated Hall-Petch relationship. The Y_2O_3 nanoparticles break down into Y and O atoms through mechanical alloying and consequently dissolve into Fe-Ni metal matrix to form a supersaturated solid solution first. The addition of Ti atoms consolidates with Y and O and re-precipitates as Y-Ti-O based nanosize complex clusters within the matrix. XRD phase analysis and TEM-SAED study confirmed the formation of complex dispersoids ($Y_2Ti_2O_7$ and TiO_2), which played an important role in hindering matrix grain coarsening. The grain size evolution was confirmed by EBSD analysis in addition to TEM. The relative sintered density of 2Ti added alloy was found to be low (96.5%) compared to 1Ti (97.7%) and 0.3Ti (98.2%) added alloys, respectively. A ball on disk wear test showed a lower wear rate for the 2Ti added alloy due to the uniformly distributed dispersoids present within the metal matrix. Corrosion-resistant of the alloys (conducted in an electrolyte of 3.5% NaCl) were found to have insignificant effect of Ti variation in the said compositions. Orowan strengthening and Zenner pinning played pivotal roles to yield high thermal stability and ultrafine structure.

Keywords: Mechanical alloying; Spark plasma sintering; Corrosion-resistant; Grain refinement; Nanosize dispersoids; Electron back-scattered diffraction.

1. Introduction

Fe-Ni alloys not only give resistance to corrosion but also resistance to thermal expansion when Ni is added in a significant amount, such as in Fe-42%Ni (super invar) and Fe-36%Ni (invar), which are the best examples for showing the least thermal expansion [1-4]. Along with these properties, the material should be capable to withstand high temperature stress and/or loading. ODS (Oxide dispersion strengthened) Fe-based alloys are known to play a very important role in this context. The morphology of dispersoid(s) formed, its shape, size, and crystal structure play very important role to impart above properties. To develop Fe-based ODS alloys and to realize its applications, it is highly important to understand the role of various elements added to it and structure of dispersoid(s) that would form with major elements [5-8]. Dispersoid formation depends on different processing condition, amount, and type of oxides added (e.g., Y_2O_3, ZrO_2, Al_2O_3 etc.) to the metal matrix along other alloying elements (Ni, Cr, Zr, Al, Ti etc.). Also, other parameters such as heat treatment conditions would result in the final microstructure of the ODS steels.

Various researchers [7, 8] have mentioned different processing conditions and the parameters responsible for the formation of dispersoids. The addition of Y_2O_3 in Fe-based alloys plays a vital role in grain refinement of the matrix, increase in the hardness and lower the average density [9]. Growth of the matrix grains is restricted and attained a stabilize refined size as Y_2O_3 particles hinder the movement of grain boundaries during recovery and recrystallization [10].

Moreover, Y_2O_3 has lubricant property and could increase the density of the processed alloy powders during compaction if added in desired amounts (up to 1.5-2 wt.%). On the other side, if Y_2O_3 is added in excess amount, it results in a decrease in the density of the compacted powders due to the distribution of Y_2O_3 particles along grain boundaries [11, 12]. Y_2O_3 powders could be decomposed into atomic Y and O through mechanical alloying and dissolve into the metal matrix simultaneously to transform into a supersaturated solid solution [13]. High energy mechanical alloying process can create high-density defects such as point defects and dislocations in the matrix that would generate favourable sites for precipitation of nanosize oxides during consolidation at high temperatures. It is reported that the addition of Ti amalgamates with dissolved Y and O atoms and reprecipitate to form Y-Ti-O complex nanosize oxides within the metal matrix [13,14]. Relatively coarser and stable $Y_2Ti_2O_7$ and Y_2TiO_5 would be evolved with a higher Y_2O_3/Ti atomic ratio, while other Y-Ti-O nanoclusters are formed with a low Y_2O_3/Ti atomic ratio.

The other Y-Ti-O nanoclusters (NCs) have coherent structure with matrix, hence requires lower formation energy compare to $Y_2Ti_2O_7$. High density of nanosize stable oxides can remarkably improve the alloy properties like, better creep resistance, toughness, and radiation resistance [5, 14, 15]. Peng et al. (2021) [16] compared the effect of Y_2O_3 and/or Ti addition in CoCrFeNi high entropy alloy (HEA) metal matrix. It was found that the addition of Y_2O_3 and Ti together, the matrix grain size becomes finer (128 nm) with simultaneous increase in hardness (637 HV) as compared to coarser grain (334 nm) and lower hardness (509 HV) in CoCrFeNi HEAs without Y_2O_3 and Ti. It could be explained that the grain size could be refined by addition of Y_2O_3 and Ti, as both constituents together resulted in strong pinning effect on grain boundaries. Oxide addition in metal matrix plays a very important role in corrosion resistant also. Perez et al. (2009) [17] studied the behavior of oxide addition on corrosion resistant. Yttria (0.6 wt.%) was introduced in Ti-based metal matrix. The samples were prepared by using powder metallurgy route involving mechanical grinding of both the elements with and without Yttria. The milled samples were first compacted with cold isostatic pressing at 250 MPa and sintered via hot isostatic pressing at 1300 °C for 4 h, and 1350 °C for 2 h with applied pressure for 200 MPa. Then the samples were subjected to thermogravimetric measurements for studying corrosion behaviour of sample. The test was conducted at the temperature range (700-900 °C) for 150 h. The exposed cross-section and surface of the samples were studied, and evaluated the deposited mass. At the temperature of 700 and 800 °C, it showed the same amount of rutile layer deposition. But there was more deposition of rutile layer on PM-Ti (Ti prepared by powder metallurgy route) sample when the test was conducted at 900 °C. The reason behind the low corrosion rate in Ti-0.6Y_2O_3 was due to low activation energy of Ti-0.6Y_2O_3 (314 kJ/mol) compare to PM-Ti (324 kJ/mol). The contribution of internal oxidation was proportionally less in Ti-0.6Y_2O_3 consolidated at 900 °C. The addition of yttria could introduce the dense oxide layer at 900 °C so that it could involve in decreasing of oxidation kinetic.

Kotan et al. (2014) [18] studied the effect of Zirconium and nanosize Yttria on thermal stability and hardness of Fe-Ni matrix. It was found that the addition of 1% Zr in Fe-Ni matrix could contribute to increase in hardness by 200% as compared to Fe-Ni alloy. Addition of 4% Zr cause to decrease in hardness by 10% as compared to 1% Zr addition. Optimization of Zr addition could help to achieve good hardness and other mechanical properties. It was found that addition of oxide (3% Y_2O_3) to the metal matrix of Fe-Ni-Zr could give around 260% more hardness as compared to Fe-Ni alloy. The reason behind this is the higher stability of well-dispersed Y_2O_3 along with second phase particles developed

($FeZr_3$, Zr_2(Ni, Fe), Fe_2Zr, $Fe_{23}Zr_6$) due to addition of Zr. Accordingly, annealing at 1000 °C showed lower hardness as compared to the sample annealed at 900 °C due to coarsening of matrix grains as second phase particles were found unstable at higher temperature.

The motivation to carry out the present work is to develop an ODS austenitic steel for high temperature applications such as fuel cladding of nuclear systems, heat exchanger, nuclear first wall reactor construction, marine parts, and critical components of chemical industries, where it is required to have high temperature stability to withstand high load, high radiation as well as corrosion resistance. Generally, invar materials start to deteriorate its low coefficient of thermal properties and mechanical properties at higher temperature greater than 250 °C [2, 3]. For invar containing 40-42% Ni alloys, various researchers [1, 4] have not found impressive mechanical properties in their studies. Some other researchers [10-12] have also reported that an increase in Y_2O_3 content in metal matrix causes an increase in hardness, but if added up to a certain extent, i.e., 2wt.%. Thereafter, there would be a declined of hardness. Hence, the optimized amount of Y_2O_3 is accepted to be as 2wt.%. Some researchers [13-15] have studied the effect of Y_2O_3/Ti ratios on the phase evolution and mechanical properties of steels. It was found that with the addition of Y_2O_3 and Ti together with a suitable ratio, the matrix grain size becomes finer and simultaneous increase in the hardness as compared to only Y_2O_3 added alloy. Researchers [13,15] showed that 1:1 (mass%) Y_2O_3/Ti atomic ratio is required to form higher number of comparatively stable $Y_2Ti_2O_7$ and Y_2TiO_5 oxides. The formation of $Y_2Ti_2O_7$ oxides was found suppressed in lower Y_2O_3/Ti ratio due to reduced concentration of Y and O. Formation of $Y_2Ti_2O_7$, Y_2TiO_5 contribute to grain refinement of the matrix and grain refinement leads to increase in strength of the alloy.
To the best our knowledge, so far, no study has been conducted to investigate the role of Y_2O_3/Ti ratio in the phase evolution of super-invar based ODS alloys, and their thermal stability. In this study the base composition of Fe-42 wt.% Ni was taken as a metal matrix and 2 wt.% nanosize Y_2O_3 oxide was added to the metal matrix with a varying amount of Ti (0.3, 1 and 2 wt.%) to design 3 compositions such as Fe-42Ni-2Y_2O_3-0.3Ti, Fe-42Ni-2Y_2O_3-1Ti, Fe-42Ni-2Y_2O_3-2Ti. This is expected to enlighten understanding the effect of Y_2O_3/Ti ratio on the evolution of microstructure of super-invar based ODS alloys, their thermal stability, mechanical properties, and corrosion behaviour.

2. Experimental details

2.1 Alloy Preparation

The blend compositions of Fe–42% Ni–2% Y_2O_3 – x% Ti (x = 0.3, 1, and 2) (Fe-10 μm, Ni-44 μm, Ti-50 μm, 99.5% purity, Y_2O_3 - 30-60 nm size prepared via ball-milling, 99.9% purity, Alfa Aesar) were mechanically alloyed with different wt.% of Ti in high energy ball-mill (8000M Mixer/Mill, USA) (for 25 h The studied compositions (i.e., Fe-42Ni-2Y_2O_3-0.3Ti, Fe-42Ni-2Y_2O_3-1Ti, Fe-42Ni-2Y_2O_3-2Ti), have been abbreviated as 03Ti alloy, 1Ti alloy, and 2Ti alloy, respectively, for the convenience. Mechanical alloying of the blend compositions was performed in a chrome-steel vial with stainless steel balls in 99.99% purity of argon atmosphere with the powder to ball of 1:10.

Table 1: Chemical composition (wt.%) of Fe-Ni based ODS alloys.

Alloy name	Ni	Y_2O_3	Ti	Fe
03Ti	42	2	0.3	Bal
1Ti	42	2	1	Bal
2Ti	42	2	2	Bal

2.2 Consolidation of the ball-milled alloys

The milled samples were consolidated and compacted by spark plasma sintering (Dr. Sinter, Japan) method in a 99.99% pure argon atmosphere. The sintering was performed using a 10 mm graphite die-punch arrangement at a temperature of 1000 ℃ with a 100 ℃/min heating rate, at an applied pressure of 60 MPa for a holding time of 5 min. Relative density of sintered samples was measured with a density measurement kit attached to a weighing balance (ML204/A01, METTLER TOLEDO, Switzerland) based on the Archimedes method.

The sintered samples were polished mechanically to a mirror finished surface using a series of emery papers followed by cloth polishing using ultrafine alumina powder. The mirror polished samples were etched using 5% Nital (95% ethanol + 5% HNO_3) solution for 5-10 seconds. The microstructure of the etched surface was captured using a light optical microscope (500 M Leica). Also, a scanning electron microscope was used to study the microstructural features of the sintered samples. X-ray diffraction (XRD) technology equipped with Rigaku x-ray diffractometer with CuKα ($\lambda = 0.154$ nm) radiation was used for studying the different phases present in the alloys. XRD data were recorded at a scanning rate of 1 °/min. The X'pert high score plus software was used to remove the background noise and thereafter phase analysis. The XRD results were plotted using Origin Pro 2018 software. Analysis of grain size, strain, phase distribution mapping, inverse pole figure mapping, and grain average misorientation of the sintered samples was studied through EBSD analysis (FEI Quanta 3d-FEG). The EBSD was performed at a scan rate of 0.05 μm. The samples for

EBSD study were prepared by polishing using a fine grade colloidal silica solution (0.02 μm). The selected sample was electropolished with an electrolyte solution (10% Nitric acid + 90% Ethanol) for the HR-TEM study. Matrix and dispersoid phase were analyzed by measuring the *d*-spacing of the phases captured by using HR-TEM (JEM 3200FS, Japan). Nanoindentation hardness and modulus of elasticity measurement of the sintered samples were carried out using a nanoindentor (Hysitron – Ti 950 Triboindentor) with an applied load of 5000 μN/s for a dwell time of 15 s. It was found that the hardness varied from the surface to a certain depth of the sample due to carbon enrichment during SPS. Hence both, top and bottom surfaces of the SPSed samples were cut off up to 0.5 mm depth to eliminate the anomalies of the hardness. Then hardness measurement was performed again.

The sintered sample were polished using various grades of emery papers (800, 1200, 1500 & 2000), and then cloth polished using ultrafine alumina powder-water emulsion. Mirror polished sintered sample was subjected to wear in a tribometer (DUCOM, Bangalore, India) with ball on disk arrangement in dry state. The sample was rotated at 500 rpm at radius of 5 mm against alumina ball (16 GPa hardness, RGP, Bangalore, India) for 30 min. Wear track groves were formed after the tests. Width and depth of wear track/grove were measured using profilometer (Mitutoyo, SJ 400, Japan) and the data was plotted using origin software. Gamry potentiostat (model: Interface1000) instrument was used to evaluate corrosion behavior of the SPSed specimens. The sintered polished sample was subjected to round bottom cell with 3.5% NaCl electrolyte solution and saturated calomel electrode as a reference electrode. After the tests completed, the corroded surface features were captured and analysed using scanning electron microscope.

3. Results and discussion

3.1 Spark Plasma Sintering (SPS)

Figure 1a shows sintering profiles during consolidation of the 03T, 1Ti, and 2Ti alloy samples sintered at 1000 °C. Each profile could be categorized into 3 stages: stage-I showing increase of temperature with corresponding displacement proportionally with progress of time up to 1000 °C. With increase in the temperature, there is an increase in diffusion rate and mass transportation to the neighbouring particles. The surface of particles becomes softer at high temperature due to which surface diffusion increases to form inter-particle bonding easily. Stage-II consists of holding period where the temperature is constant at 1000 °C. In this stage, there is almost no change in the displacement. It means no effect on consolidation

through diffusion in this period. Stage-III is the final stage where cooling of the system occurs, which is also reflected in the decreasing temperature profile. The SPS machine is equipped with optical pyrometer for detection of temperature. Optical pyrometer is often used for detection of high temperature, and this may not be able to detect lower temperature. Once the temperature is reached 600 °C, then pyrometer could effectively be able to detect the actual temperature of the furnace/sample. After detection of temperature, program input temperature through software and actual temperature both follow up together to achieve the required heating rate [19]. Therefore, heating rate below 600 °C is not properly detected as shown in Fig. 1a.

It is found that there is an increase in displacement with decrease in the temperature. The reason behind this is the shrinkage of the die-punch arrangement as well as in the sample [4, 20]. Due to the formation of more and homogenously distributed dispersoids in the sample of 2Ti alloy, the displacement is found to be low (3.87 mm) as compared to that in the 03Ti alloy (4.6 mm) and 1Ti alloy (4.28 mm). Formation of the nanoscale oxides/dispersoids could restrict grain coarsening and result in finer grains structure in the 2Ti alloy.

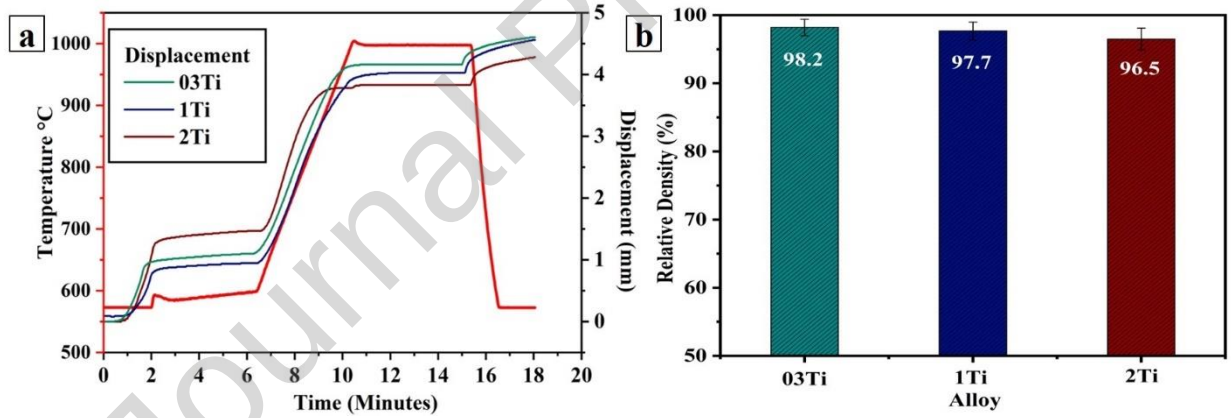

Fig. 1: (a) SPS profile between temperature, displacement and time during consolidation of the 03T, 1Ti, and 2Ti alloy, (b) Relative density of different alloy compositions SPSed at 1000 °C.

Prior to the measurement of sintered density, certain amount of material (i.e., 0.5 mm) was sliced out from both ends of the cylindrical SPSed samples. The reason behind this is the carbon diffusion (from the graphite punch) into the flat surface of the cylindrical specimen to a certain depth while sintering. The same issue (i.e., carbon diffusion) was also reported in [21]. Fig. 1b shows the relative sintered density of 03Ti, 1Ti, and 2Ti alloy, sintered at 1000 °C. It was found that the samples with higher Ti content (2Ti alloy) were found to yield a lower density of 96.5%, as compared to other alloys, 03Ti (98.2%) and 1Ti (97.7%). This is due to the evolution of more amount of nanoscale dispersoids in 2Ti alloy, such as $Y_2Ti_2O_7$

and TiO_2. As these dispersoids are stable even at higher temperature, they consequently restrict grain growth as well as create obstacles for the consolidation, which decreased in the sintered density [22, 23].

3.2 X-ray diffraction phase analysis

XRD patterns of the milled and sintered samples with different percentages of Ti are shown in Figs. 2a & 2b, respectively. The diffraction peaks of the milled alloys become broader and shorter in peak intensity (Fig. 2a). The reason behind this is the decrease in the crystallite size and increase in the internal lattice strain after mechanical alloying. The mechanically alloyed samples showed the major peaks of Fe-Ni FCC (Austenitic) (00-047-1417) in case of all three alloys. Whereas in the 2Ti alloy additionally showed the presence of $Y_2Ti_2O_7$ pyrochlore phase (01-071-2065) and, orthorhombic TiO_2 phase (01-076-1935). Some researchers [4, 24, 25] have shown that after 25 h of milling, the added Y_2O_3 dissolved and distribute uniformly in the matrix.

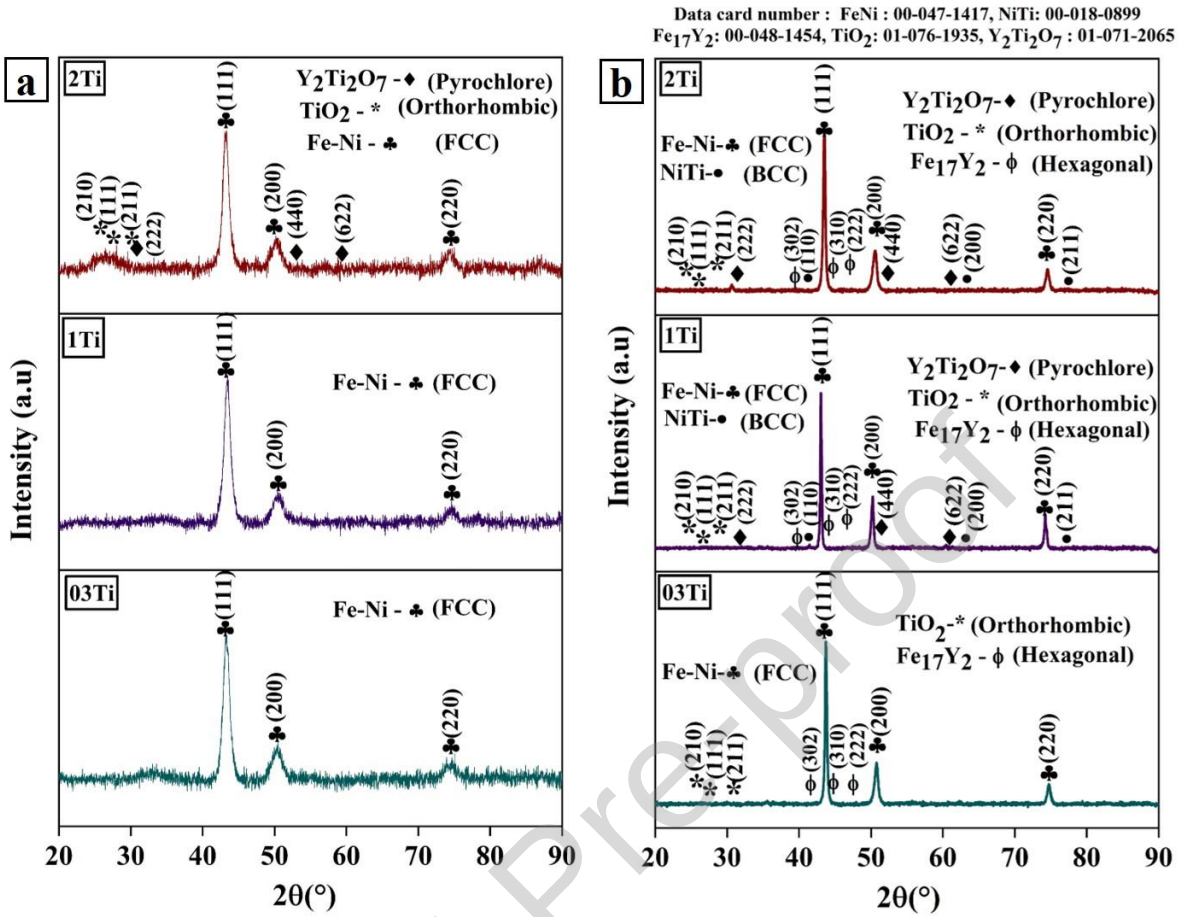

Fig. 2: X-ray diffraction (XRD) pattern of the milled and sintered samples at 1000 °C; (a) Milled sample of 03Ti, 1Ti and 2Ti alloy. (b) Sintered sample of 03Ti, 1Ti and 2Ti alloy.

During MA for 25 h, Y_2O_3 was decomposed into atomic Y and O, and simultaneously dissolved into the metal matrix to form a supersaturated Fe-Ni based solid solution. After the optimum time of MA, each powder particle thoroughly could achieve equivalent chemical composition, although matrix grains may not achieve homogeneity at atomic level. It required further milling, so that numerous vacancies and other defects could be created within the grains by continuous welding/re-welding and shearing/fragmentation processes [26, 27, 28]. These created vacancies empower a fast diffusion at the atomic level and form a complete supersaturated solid solution with Y and O, if sufficient activation energy is provided/achieved. The high-density defects such as dislocations, vacancies and point defects in the matrix provide preferred precipitate sites for the formation of nanoscale oxides [28, 29]. The availability of Ti atoms combines with the dissolved Y and O, and re-precipitate as Y-Ti-O nanoscale oxides in the matrix [17, 30]. Y_2O_3/Ti ratio plays a very important role in the evolution of nanoscale oxides. It was found that the formation of $Y_2Ti_2O_7$ and TiO_2 were favorable with higher Y_2O_3/Ti weight ratio, and also confirmed in the XRD patterns as shown in Fig. 2b.

Due to abundantly available Ti, Y, O in the 2Ti alloy, there was sufficient amount of TiO_2, $Y_2Ti_2O_7$ precipitates formed as compared to that in the 1Ti and 03Ti alloys. In the case of 03Ti and 1Ti alloy, Y-Ti-O based oxide formation is not detected as per the XRD analysis due to significantly lower amount availability of Ti [8, 12, 13]. It is also to note that there is a limitation of detectability by XRD. Generally, XRD could detect the presence of a phase if at least 2% of that particular phase is present in the material being studied [21]. In, XRD patterns of 03Ti, 1Ti, and 2Ti alloy sintered at 1000 °C are shown in Fig. 3b. Some new intermetallic phases namely, BCC NiTi phase (00-018-0899) and hexagonal $Fe_{17}Y_2$ phase (00-048-1454) were found to evolve. The reason behind is more solubility of element at the higher temperature. It is to be noted that all three alloy compositions (containing >50% BCC metal (i.e., Fe) gradually transformed into a Fe-Ni based FCC phase as detected by XRD (Fig.2a & b) [1, 30]. The reason behind the formation of the FCC phase is Ni, as Ni is known as FCC (Austenitic) stabilizer, and the addition of Ni to Fe greater than 20 wt.% enhance the formation of the FCC phase [31].

3.3 Microstructural study by TEM and HR-TEM

Figure 3 shows TEM analysis of the 2Ti alloy samples sintered at 1000 °C. It could be noted that there is a grain size distribution from 200 nm to 1 µm size, in which nanosize second phase particles are distributed throughout the Fe-Ni metal matrix. TEM SAED pattern in Fig. 3b confirms the formation and distribution of intermetallic phase like $Fe_{17}Y_2$, NiTi, and nano-oxide phases TiO_2, $Y_2Ti_2O_7$ within the metal matrix. The same was also confirmed by the XRD analysis as described in the section **(3.2).** Fig. 3c & Fig. 3d show the STEM and HADF image of Fig. 3a, which gives a clearer picture of the matrix grain sizes and presence of second phase particles.

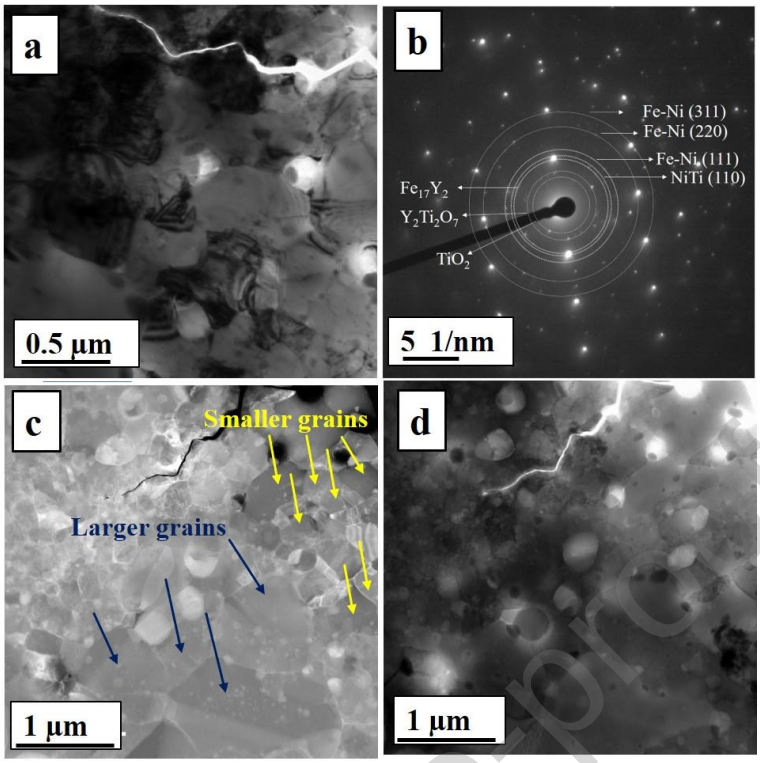

Fig. 3: Transmission electron microscopy (TEM) images of 2Ti alloy, SPSed at 1000 °C: (a) Bright field image, (b) SAED pattern, (c) corresponding Scanning transmission electron microscopy (STEM) image, (d) High angular dark filed image (HADF).

Figure 4 shows HRTEM image of the 2Ti alloy sample sintered at 1000 °C. From Fig. 4a, it can be seen that nano-oxide dispersoids are distributed in the Fe-Ni based metal matrix. The magnified images with lattice fringes of the dispersoids are shown in Figs. 4b, c and d. Fringes were measured by using GATAN software. The lattice fringes shown in Fig. 4b are analyzed to measure the inter-planar distance of 3.43Å, which is correspond to (111) of TiO_2 phase. Similarly, evolution of $Y_2Ti_2O_7$ nanosize precipitate is confirmed with the lattice fringe's width of 2.9 Å corresponding to (222).

The evolution of fine matrix grains is attributed to the formation of nanoscale second phase particles, which are dispersed throughout the metal matrix thereby creating a hindrance against grain growth at a higher temperature. Various researchers [32-34] have reported that a metal matrix can show magnificent thermal stability when nano-oxide dispersoids are present in the matrix. The presence of these oxide particles can clearly be seen in Figs. 4(a-d). It can be confirmed that these oxides are in the range of 30-50 nm. When precipitate cutting becomes difficult, dislocations move around the precipitates and bypass after making loops around the second phase particles. Thus, it is expected that these nanoscale precipitates contribute to the Orowan as well as dislocation strengthening [35-37].

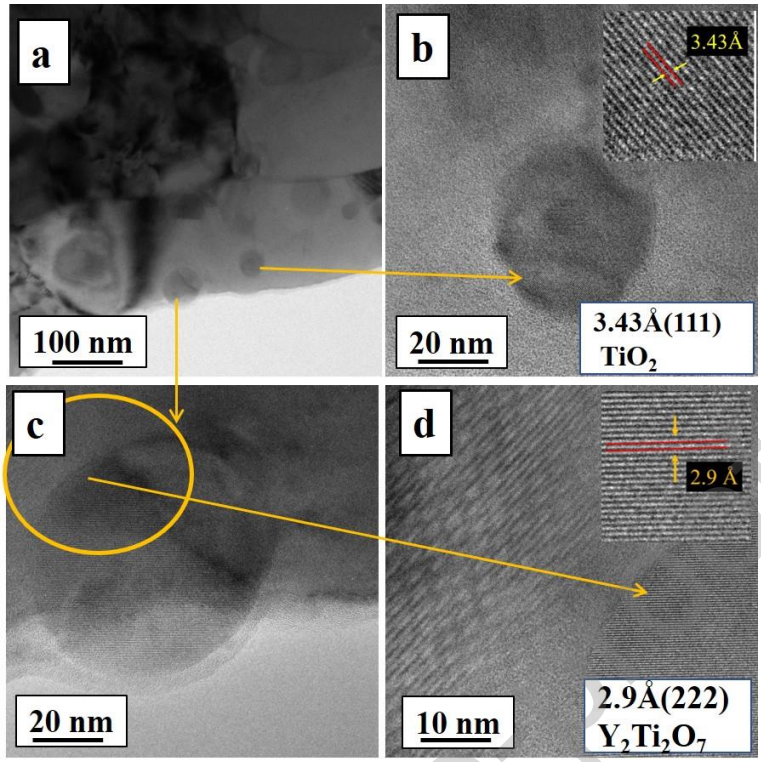

Fig. 4: HRTEM images of 2Ti alloy, sintered at 1000 °C: (a) Nano-oxide dispersoids in metal matrix, (b), (c) and (d) shows the fringes formation in nano-oxide.

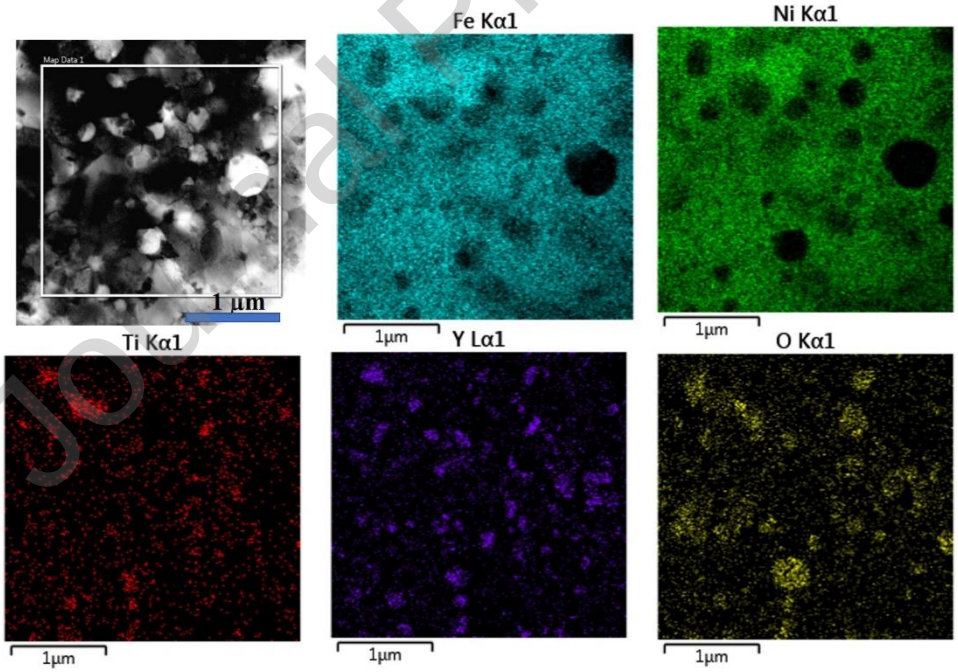

Fig. 5: Scanning transmission electron microscopy (STEM) images and EDS elemental mapping of the 2Ti alloy sintered at 1000 °C.

Figure 5 shows STEM images along with EDS elemental mapping indicating the presence of nanoscale particles present in the Fe-Ni austenitic matrix. It can be noted from the mappings of Y, O, and Ti elements that there are some small size adhered Y-based clusters present, which confirms the formation of Y-Ti-O nanoclusters. Similarly, presence of some other

phases such as $Fe_{17}Y_2$, TiO_2 could also be recognized from the EDS mappings of the corresponding elemental distribution (from Figure 5). These analyses also support the results obtained by XRD (Fig. 2) and TEM-SAED pattern analysis (Fig. 3).

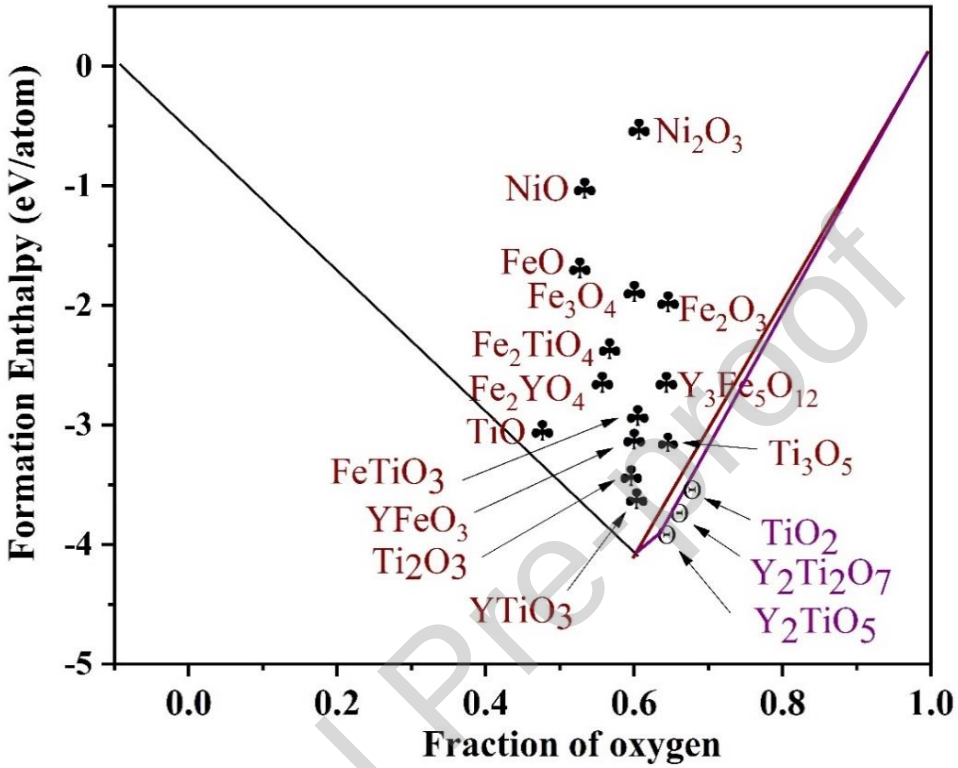

Fig. 6: Pseudo-convex-hull plot of enthalpy formation shows the oxides in Fe-Ni-Y_2O_3-Ti based alloy system, plotted as a function of oxygen fraction. Reproduced from [38, 39].

The pseudo convex-hull plot for the enthalpy formation is shown in Fig. 6, which is reproduced from [38, 39]. It is evident that Fe-O, Ni-O, Fe-Ti-O and Y-Fe-O oxides have comparatively lower formation of enthalpies, and they fall away from the convex-hull. Therefore, these oxides are considered to be less stable. On the other hand, the Y-Ti-O-based nanoscale oxides, which are observed in the 1Ti alloy and 2Ti alloys, are believed to be more stable because they are on the ground state of the convex-hull plot of Fe-Ni-Y_2O_3-Ti system. The homogeneous distribution of Y-Ti-O-based dispersoid in the Fe-Ni FCC matrix is expected to improve the mechanical properties. The significant changes in the mechanical properties and corresponding microstructure have been discussed in a later section.

3.4 Micrograph characterization based on EBSD

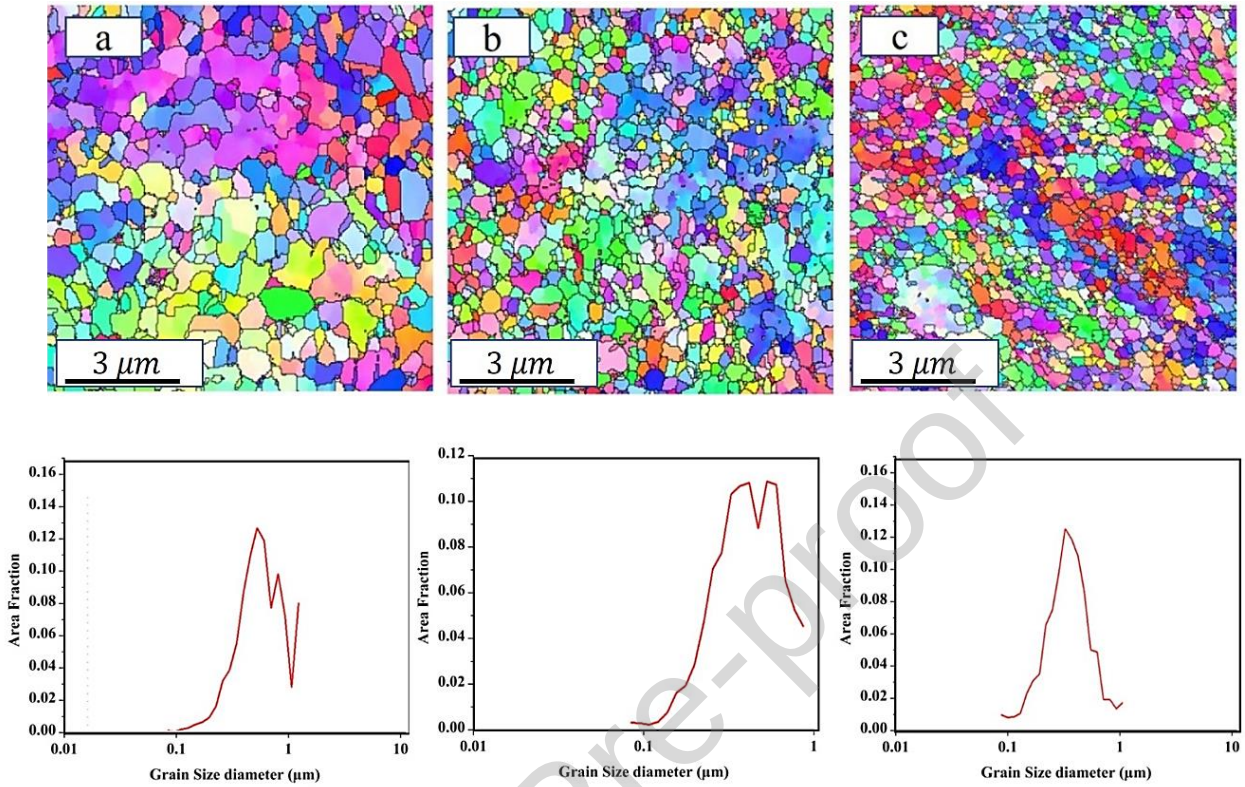

Fig. 7: (a-c) Inverse pole figure (IPF) map and corresponding grain size distribution chart (area fraction) obtained from EBSD scans taken from (a) 03Ti, (b) 1Ti, (c) 2Ti, samples, respectively.

EBSD analysis was performed and analyzed to understand the thermal stability of the SPSed samples of all three compositions. Figs. 7(a-c) show IPF maps, revealing microstructural features with grain size distribution for the sintered (at 1000 °C) samples of (a) 03Ti, (b) 1Ti, and (c) 2Ti, respectively. It is to be noted that the more uniform finer grain size (205 nm) is obtained in the SPSed sample of 2Ti alloy as compared to the larger grain size for the 03Ti (348 nm), and 1Ti (240 nm) alloys. It could be noted that the alloy with a higher Ti is thermodynamically more stable than the low Ti content alloys [32, 34]. A higher amount of Ti seems to be encouraging in the formation of higher amount complex but stable oxides which are uniformly distributed in the alloy matrix. The formation of nanoscale dispersoids was also detected through XRD and TEM analysis as discussed in section **3.2 and 3.3**. As these dispersoids are more stable at a higher temperature, it results in the evolution finer grains through precipitation/dispersion strengthening.

3.5 Phase map and KAM (Kernal Average Misorientation) analysis based on EBSD

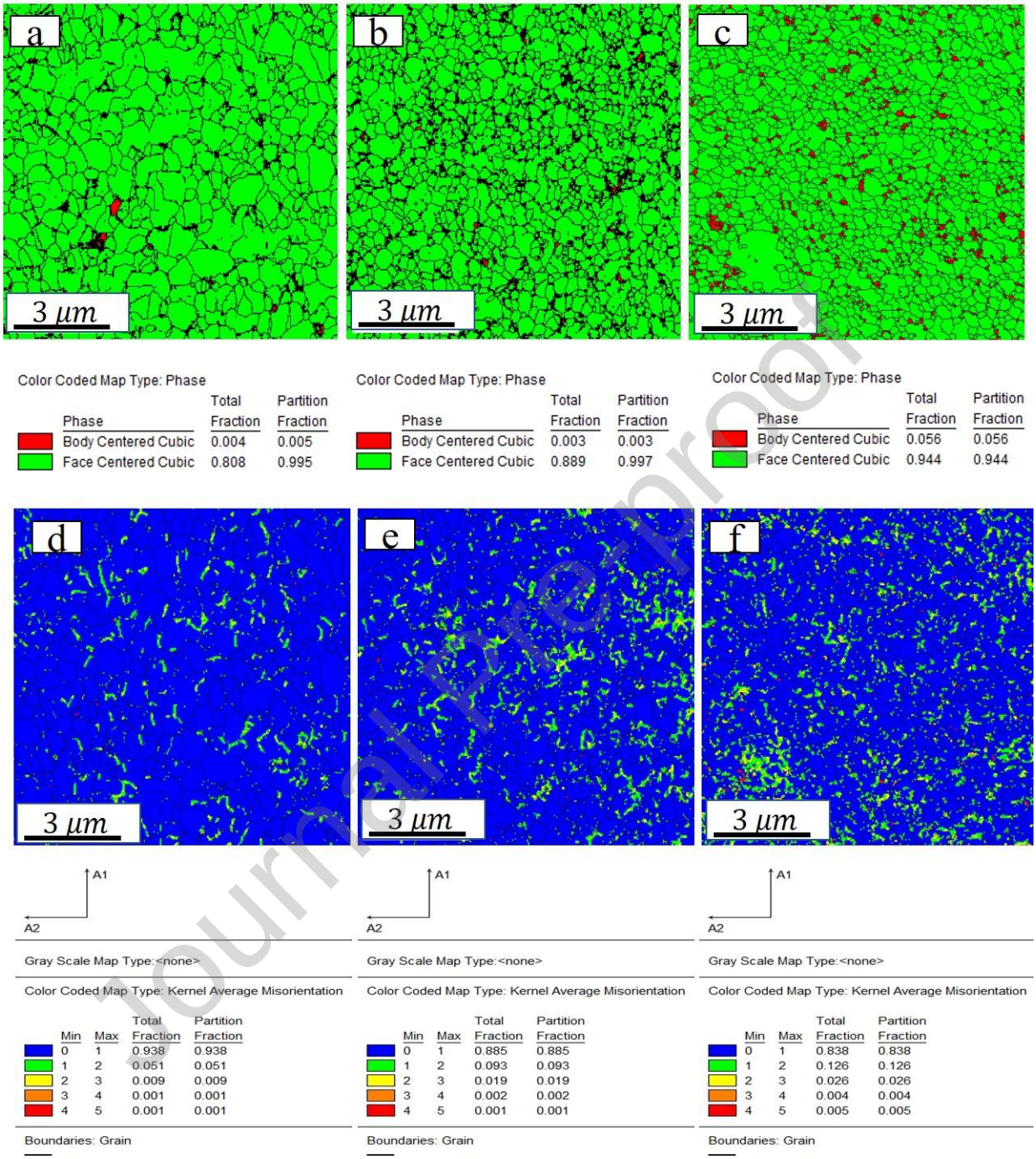

Fig. 8: (a-c) Phase map and, (d-f) KAM (Kernel Average Misorientation) map of the SPSed samples for 03Ti, 1Ti, and 2Ti alloys, respectively.

Figures 8a-c show phase maps of the SPSed samples of 03Ti, 1Ti, and 2Ti alloys, respectively. It can be observed that the Fe-Ni alloys resulted in the evolution of 99.7 % FCC+ 0.3% BCC phases, and 99.5% FCC+ 0.5% BCC phases, respectively, with addition of 03% Ti and 1% Ti. On the other hand, as the percentage of Ti increased to 2%, there is a significant increase of the BCC phase in the evolution of microstructure (94.4 % FCC+5.6%

BCC) of 2Ti alloy. Addition of 2% Ti in alloy gives rise to the evolution 5.6% BCC phase as Ti is a ferritic stabilizer [40, 41]. Ni and Ti together forming NiTi precipitates which has BCC structure, as the Ti amount is increasing, a fraction NiTi phase is also involving in formation of BCC phase. Presence of NiTi precipitate was confirmed with XRD and TEM in Figs. 2 & 3 respectively. NiTi phase was not found in XRD after milling, but detected after sintering, the reason behind is that NiTi form at temperature above 600 °C [42, 43].

Figures 8d-f represent KAM (Kernel Average Misorientation) images of 03Ti, 1Ti, and 2Ti alloy, respectively. The micro-strain in an alloy is estimated through KAM, and it is known that the presence of higher dislocation density leads to higher micro-strain [35]. The amount of microstrain has been shown in a fraction value at the bottom part of each image. It can be observed that the microstrain (represented by green- + yellow-coloured fractions:1-2° + 2-3°) is comparable in all three compositions [44]. It may be noted that the fraction (between 1-2° + 2-3°) gradually increased with an increase in the Ti content (i.e., 6% for 03Ti, 11.2% for 1Ti, and 15.2% for 2Ti alloys). It can be understood that with the increase in Ti amount, there is an increase in the formation of nanoscale second phase precipitates and oxides, which lead to accumulate higher dislocation density/microstrain. Therefore, a better dislocation density in high Ti content alloy could create more hurdles to bypass themselves, which ultimately can contribute more dislocation strengthening in it.

3.6 Texture analysis based on EBSD

Figure 9 shows pole figure maps for the SPSed samples of (a) 03Ti, (b) 1Ti and (c) 2Ti alloys, respectively. The load during SPS (at 1000 °C) was applied perpendicular to the scanned surface of the sample. The texture was calculated in percentage, using TSL OIM software and arranged in tabular form as shown in Table 2 for the convenience.

The rotated cube texture and cube texture of the 03T, 1Ti and 2Ti alloy SPSed samples are estimated to be (17.6%, 9.6%), (7.5%, 2.6%) and (2.6%, 0.1%), respectively. Various researchers [45-47] have mentioned that the addition of Ti increases amount of accumulated strain in the matrix. The strain led to increase stress and stress could hinder the dynamic recrystallization of the matrix. Thus, cube texture could be reduced with increase amount of Ti. In our study, we also found that with the increase in the Ti content, increase in micro-strain has been observed (as shown in Figs. 8d-f.) consequently with decrease in dynamic recrystallization. Alloy with low dynamic recrystallization has comparatively low cube, and rotated cube texture, but shows better mechanical properties. Brass texture for 03Ti, 1Ti and

2Ti is 3.2%, 4% and 10% respectively. Formation of brass texture depends on two main factors, i) grain size, ii) stacking fault energy. Studies [48,49] revealed that matrix with finer grains would have stronger brass texture compare to coarser grain matrix, and alloy with lower stacking fault energy is generally more dominant to brass texture. In this study, the 2Ti alloy has finer grain size, therefore has stronger brass texture as compared to 1Ti and 03Ti alloy samples. Addition of Ti, lower the stacking fault energy of the alloy and could promote brass texture [49]. Addition of Ti also affects copper texture and thereby mechanical properties. Geng et al. (2021) [50] showed that Ti added alloys have higher copper texture as compared to non-Ti added alloy, and stronger copper texture could improve mechanical properties. In the present study, 03Ti has 11% copper texture compare to 1Ti (15%) and 2Ti (28.7%). Accordingly, 2Ti alloy showed better mechanical properties as discussed in subsequent sections **3.7 & 3.8**. It could be noted that, in the present study, no relationship is found on the S, and Goss type texture evolution due to Ti variation. It could be understood that S, Cu and Goss texture are randomly distributed within the matrix.

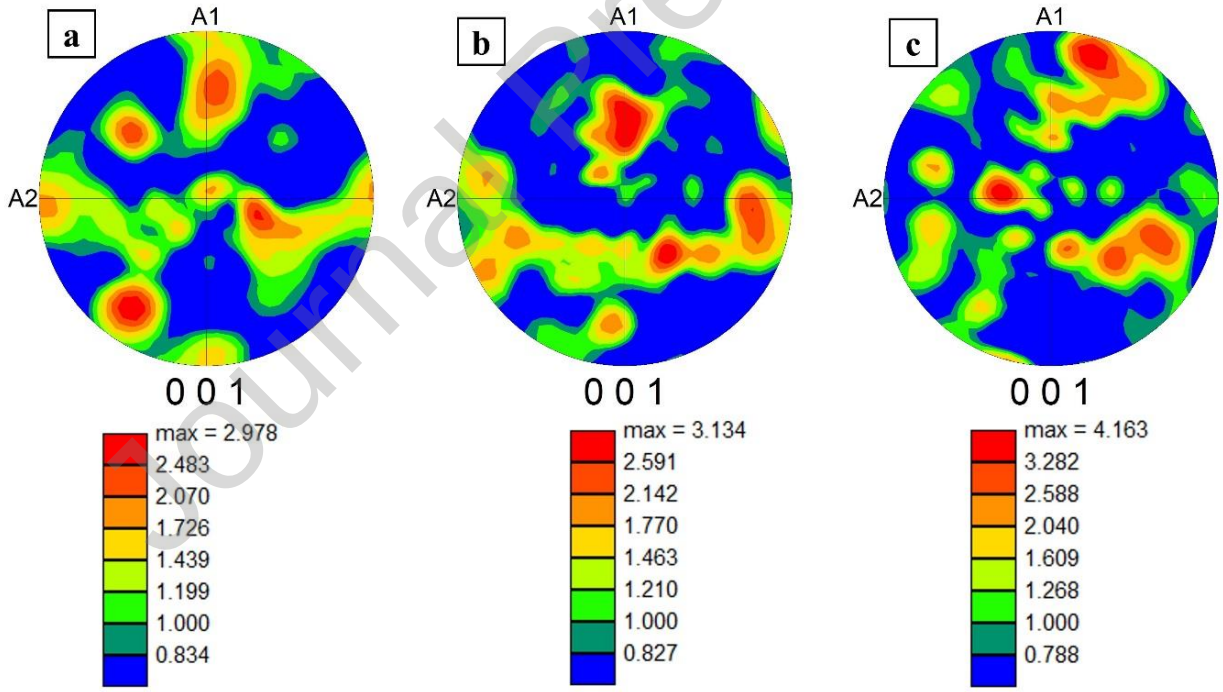

Fig. 9: 001 pole figure map obtained from EBSD scan for (a) 03Ti, (b) 1Ti and (c) 2Ti alloy, respectively.

Table 2: The calculated texture in percentage for all the SPSed samples.

Texture in %	03Ti	1Ti	2Ti
Rotated cube	17.6	7.5	2.6
Cube	9.6	2.7	0.1
Brass	3.2	4	10
Copper	11	15	28.7
S	3.1	3.5	3.4
Goss	2.9	5.2	3.7

3.7 Mechanical properties analysis

Figure 10a shows nanoindentation hardness values of the 03Ti, 1Ti, and 2Ti alloy SPSed at 1000 °C along with their corresponding elastic modulus. Fig. 10b shows loading-unloading profile of the respective SPSed sample. It is known that hardness of any sample is inversely proportional to the depth of indenter through sample [21]. The nanoindentation hardness and elastic modulus are found to increase with increase in the Ti content. The nanoindentation hardness 03Ti SPSed alloy is found to be 4.2 GPa compared to 4.5 GPa for 1Ti, and 5.2 GPa for 2Ti alloy. Similarly, the elastic modulus of 03Ti alloy is 159 GPa while it is 162 GPa for 1Ti alloy, and 167 GPa for 2Ti alloy.

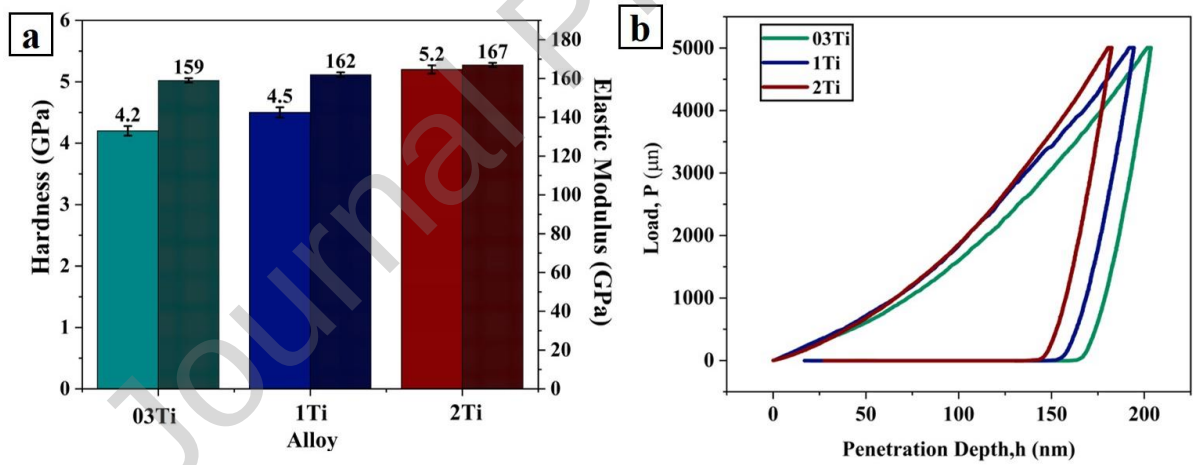

Fig. 10: (a) The Nano-indentation hardness and, (b) The loading-unloading profile obtained from nano-indentation test on 03Ti, 1Ti and 2Ti alloy.

The pattern of increasing hardness value with an increase in the Ti content was also reported in several research studies [51, 52]. This might be due to the surge in the density of the nanoscale scale precipitates/intermetallic phases formed due to a higher amount of Ti. In XRD and TEM analysis described in sections **3.2 and 3.3**, it was observed that intermetallic phase $Fe_{17}Y_2$, NiTi, and nano-oxide precipitates $Y_2Ti_2O_7$ and TiO_2 are formed in 1Ti and 2Ti alloy. From EBSD analysis described in section **3.4**, it was confirmed that Ti addition in the matrix is acting as a barrier to grain growth and refining the Fe-Ni matrix grains. It could also

be seen that with addition of more Ti, there is a grain size reduction, which showed the finest grain size of 205 nm in the 2Ti alloy compared to 348 nm in 03Ti, and 240 nm in 1Ti alloy. Hence, the variation of hardness and elastic modulus values is highly correlated with the corresponding morphology and microstructural features of the SPSed samples.

3.8 Wear Behavior

The wear testing of the sintered samples was performed by using a ball-on-disc wear testing system. A polished surface of the SPSed samples (03Ti, 1Ti, and 2Ti) was encountered against 10 mm alumina ball. It could be observed from Fig. 11(a) that the wear rate of both the alloys gradually increased with testing time. Alloy with a low Ti content 03Ti showed maximum wear of ~102 μm in comparison to the ~45 μm for the 2Ti alloy and 73 μm for the 1Ti alloy, respectively. It seems that the sample of greater hardness shows higher wear resistance. The important reasons for achieving higher wear resistance are grain refinement, alloying, surface modification, plastic deformation, etc. The grain refinement method has been widely studied in engineering materials in the essence of the Hall-Petch relation (i.e., flow stress dependence of grain size) [53, 54]. It is to be noted that the sample of 03Ti has a larger grain size of 348 nm compared to a grain size of 240 nm of 1Ti alloy and 205 nm for the 2Ti alloy. This indicates that the wear rate of the SPSed samples is followed as per the Hall-Patch relation. It has already been described that the addition of Ti played an important role in achieving grain refinement [55]. It is also observed from the analysis of XRD and TEM results that the addition of Ti in the Fe-Ni-Y_2O_3 alloy could give a boost in the formation of nanoscale precipitates ($Y_2Ti_2O_7$ and TiO_2). The hard complex nanoscale precipitates uniformly distributed in the 2Ti alloy not only played a vital role to refine the matrix grains but also increased the hardness significantly resulting a low wear rate (i.e., better wear resistance).

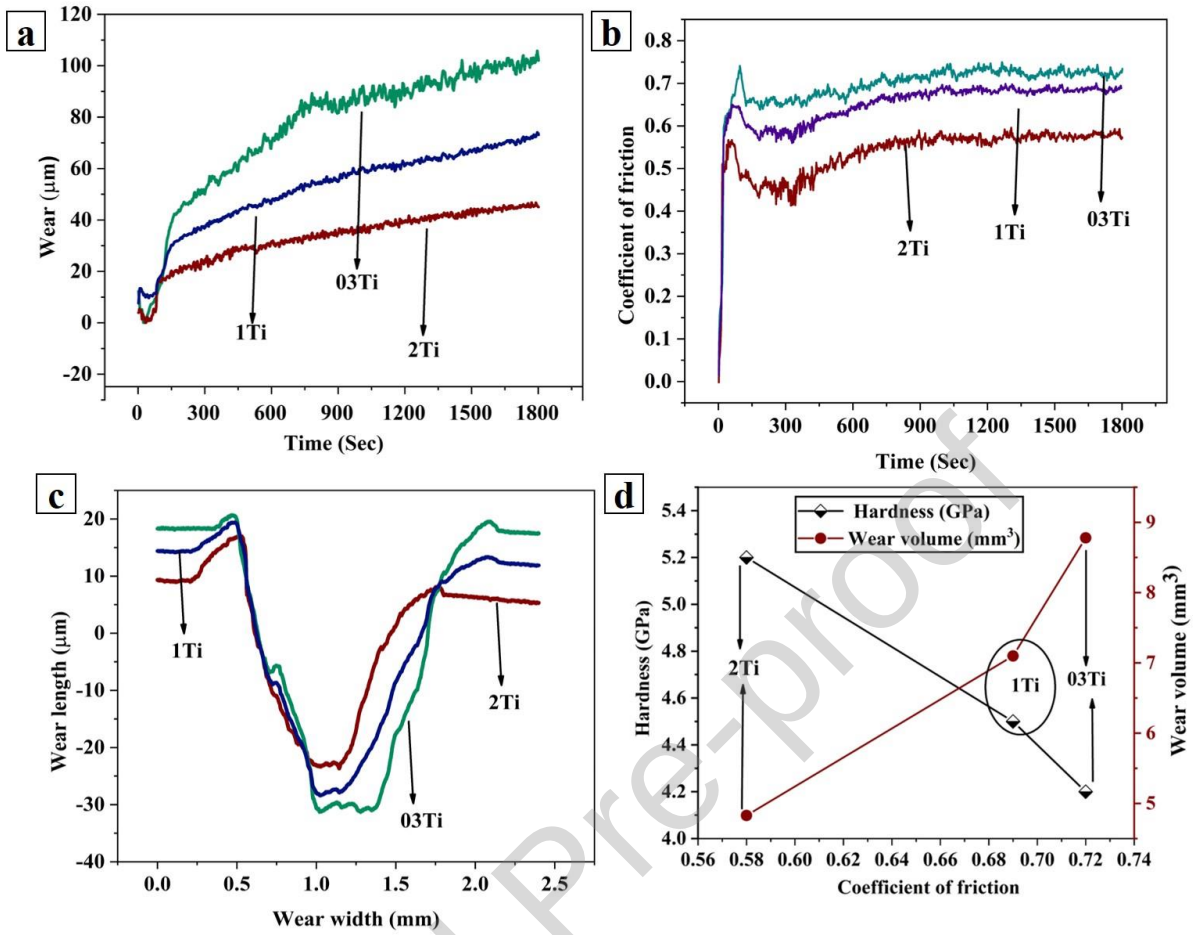

Fig.11: Variation in (a) wear vs. time (b) COF (coefficient of friction) vs. time and, (c) wear length vs. wear depth of SPSed 03Ti, 1Ti and 2Ti alloys at an applied load of 10 N, (d) plotted graph based on Archard's equation.

Figure 11b represents change in the coefficient of friction (COF) with testing time. The result shows that the COF is low (0.58) for the 2Ti alloy as compared to 0.69 for 1Ti alloy and 0.72 for the 03Ti alloy. The reason for the low COF is the formation of adherent and strain-hardened tribo-layered structure that could prevent further wearing of the metal matrix in the 2Ti alloy [53]. Fig. 11c represents the consequent results from Figs. 11a and 11b, showing the comparative plot of wear depth vs. wear width measured using a profilometer. The wear-out area is measured using the mathematics of integration function in origin software and mentioned in table 3. The total track diameter is 6 mm. Total wear out volume in mm^3 = wear out area $\times \pi \times 6 /100$. It could be seen that the wear-out volume decreases with increase in the Ti content, which is also confirmed with Figs. 11a, and 11c, respectively.

Table 3: Total wear out area and wear out volume of the SPSed samples

Alloy	Wear out area in μm^2	Wear out volume in mm^3
03Ti	1676	8.78
1Ti	1356	7.10
2Ti	922	4.83

Figure 11d shows that the plotted graph based on Archard's equation. It is well known that materials under same conditions, with higher hardness are more resistant to wear compared to softer materials [56, 57]. Influence of hardness on the wear volume (Q) is described by Archard's equation [57] as follows:

$$Q = K\frac{W}{H}$$

Where, Q is the wear volume per unit sliding distance, K is the coefficient of wear/friction, W is the applied load, and H is the hardness of the sample, which is obtained from nanoindentation test.

The graph shown in Fig. 11d indicates the variation in wear volume and hardness with respect to coefficient of friction. The SPSed samples have been marked corresponding to their wear volume and their hardness values [56]. The 03Ti, 1Ti and 2Ti alloy samples have hardness of 4.2, 4.5 and 5.2 GPa, respectively, against their corresponding calculated wear out volume of 8.78, 7.10, and 4.83 mm^3. The 03Ti sample has lower hardness value consequently showing higher wear out volume as compared to 1Ti and 2Ti alloy samples. It can be noted that volume loss is inversely proportional to the material's hardness. Same pattern is found to follow by all the alloys, which also supports Archard's equation as well.

3.9 Corrosion behaviour

Figure 12 shows the Tafel plot obtained from polarization tests of the SPSed samples in a 3.5% NaCl electrolyte solution. The corrosion occurs on the surface of the sample due to potential difference between cathode and anode. Formation of galvanic cells generate potential difference. If the sample is corrosive resistant it means potential difference between cathode and anode is low. In our study, working sample acted as an anode, it means oxidation/anodic reaction would occur on the sample only. Whereas electrolyte solution (i.e., sodium chloride in distilled water) would act as cathode, where cathodic reaction or reduction would occur on it. Relatively more passive element is used as cathode so that anode can release the electrons in the electrolyte solution and cause rusting [58, 59]. The corresponding

E_{corr}, E_{pit} and I_{corr} values are extracted using Tafel extrapolation method from the polarization curves and mentioned in Fig. 12 and tabulated in Table 4 for better understanding. The pitting potential (E_{pit}) has been determined using anodic polarization curve of Tafel polarization plot and has been marked against their corresponding alloy sample. The E_{pit} value of the 03Ti, 1Ti and 2Ti samples are -5.2 mV, 54.1 mV and 41.6 mV, respectively. Higher E_{pit} value is the significance of higher passivity, it means the alloy is more adherent to corrosion resistance due to its passive nature [55].

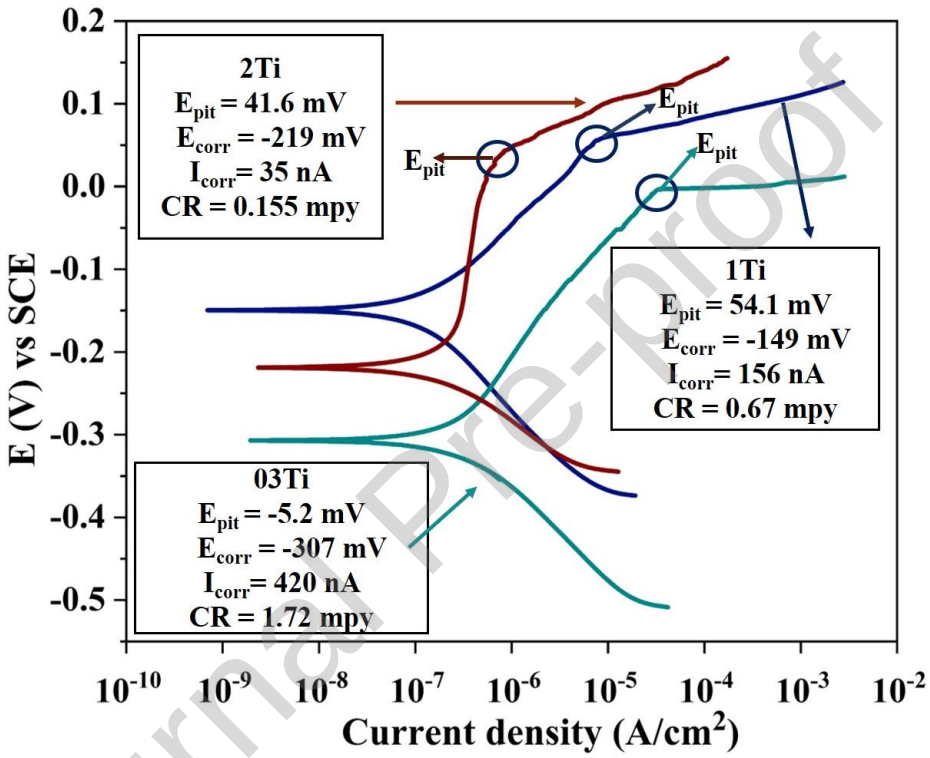

Fig. 12: Potentiodynamic polarization scans of the 03Ti, 1Ti, and 2Ti alloy samples sintered at 1000 °C. E_{pitt}, E_{corr}, I_{corr} and CR (Corrosion rate) values has been mentioned and marked against each alloy.

Table 4: Calculated values of I_{corr} and E_{corr} of the SPSed samples obtained from Tafel polarization curves. Corresponding to corrosion rate (CR) value obtained from above given formula.

Alloy	I_{corr}	E_{corr}	CR (mpy)	E_{pit}
03Ti	420 nA	-307 mV	1.72	-5.2mV
1Ti	156 nA	-149 mv	0.67	54.1mV
2Ti	35 nA	-219 mV	0.155	41.6mV

E_{corr} value signifies the corrosion resistance or corrosion tendency of the sample, whereas I_{corr} value quantifies the corrosion rate. The corrosion current density, I_{corr}, is 420 nA/cm^2 for the 03Ti alloy, which is more as compared to 156 nA/cm^2 of the 1Ti alloy and only 35 nA/cm^2 for the 2Ti alloy sample. The evaluation of corrosive properties reveals that Ti addition can

efficiently increase the pitting potential and widen up the passive region. Pitting potential increases, and pitting size decreases with the increase of Ti content [60]. The CR value for all the alloys was determined using the following formula [61].

$$\text{CR (mpy)} = 0.13 \times \text{I}_{\text{corr}} \left(\frac{\mu\text{A}}{\text{cm}^2}\right) \times \text{ [eqv. weight of sample / Density of sample]}$$

The improvement in corrosion resistance value is accomplished with addition of Ti, which possibly could influence I_{corr} value. It can be observed that CR is directly proportional to I_{corr} value. Although it depends on density and equivalent weight of sample, but these values are having very less difference as sintered conditions were same for all three alloys.

Recent studies [62, 63] described the corrosion rate in the form of an Arrhenius equation as follows:

$$k_p = k_o \exp(-\frac{Q}{RT})$$

Where, k_p is the effective corrosion rate, Q is the activation energy of the oxidation reaction, k_o is the rate constant, and R is the universal gas constant, and T is absolute temperature. Equation relates the corrosion rate with oxidation reaction, and oxidation reaction depends on diffusion mechanism. They [62, 63] have found that k_p value of Y_2O_3 based alloy is 4 times larger as compared to that in a Ti-added Y_2O_3 based alloy. In our case, the corrosion rate for the 03Ti, 1Ti and 2Ti alloy samples is 1.72, 0.67 and 0.155 mpy, respectively. It could be seen that with addition of Ti amount in Y_2O_3 based ODS steel, the corrosion rate decreases. Based on Arrhenius equation, Y-Ti-O possesses a higher oxidation activation energy than Y_2O_3. The oxidation reaction usually occurs due to the diffusion of metal cations to the water-oxide interface or due to the diffusion of oxygen anions to the oxide-metal interface. This means that the diffusion of metal cations and/or oxygen anions through the oxide layer in Y-Ti-O (due to higher oxidation activation energy) is more difficult to take place than in Y_2O_3. This explains why 03Ti alloy sample performs worse than the 2Ti alloy in 3.5% NaCl corrosive environment.

Fig. 13 shows SEM images of the SPSed samples scanned after the corrosion polarization test in 3.5% NaCl solution. The scale bar on Fig. 13a is kept as 100 μm, because the number of pits on it is so high that these were not properly visible on higher magnification as that shown in Figs. 13c & d (like similar 2 μm scale bar). The intensity of pits formation in 03Ti alloy

(Fig. 13a) can be seen more compared to that in the 1Ti alloy (Fig. 13c) and 2Ti alloy (Fig. 13d). Along with the number, size of pits is also observed to be less in the 1Ti and 2Ti alloys as compared that in the 03Ti alloy. The magnified image of Fig. 13a shows the formation of corrosion pitting and corrosion products (shown in Fig. 13b), which were formed after the polarization test. It also confirms that the lower I_{corr} value in the 2Ti alloy reveals less number and smaller size corrosion pitting as shown SEM image (Fig. 13d), compared to 03Ti (Fig. 13a) and 1Ti (Fig. 13c).

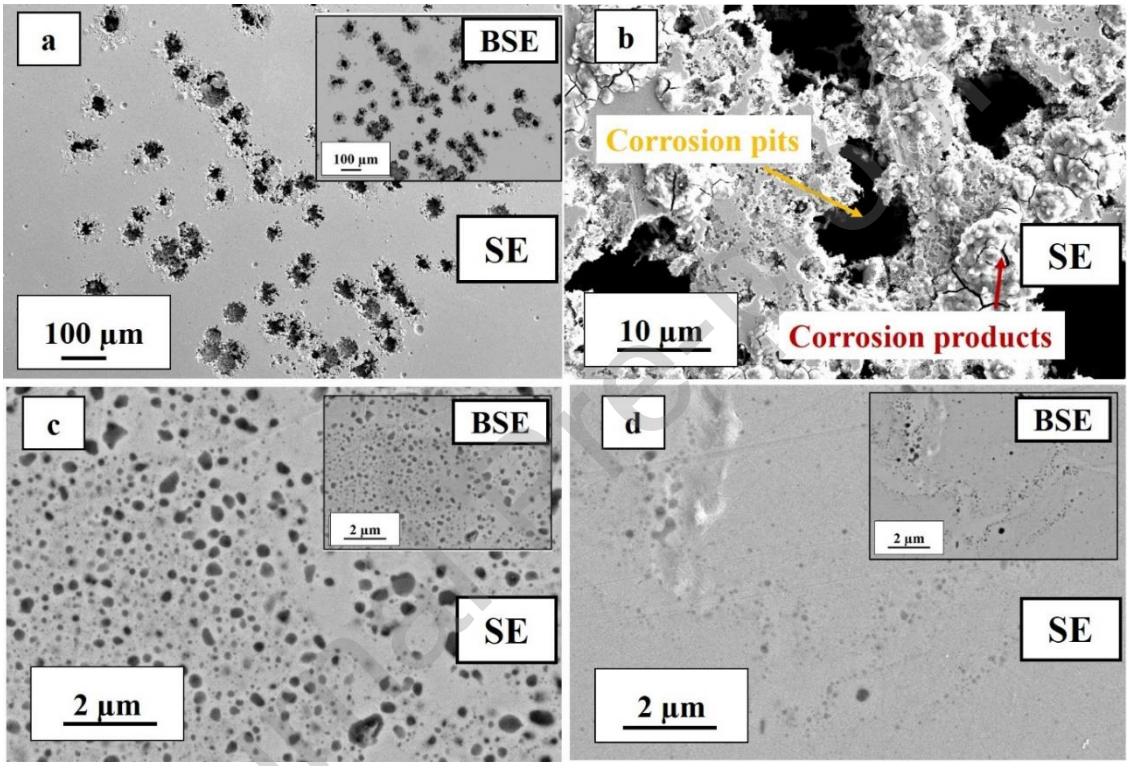

Fig. 13: SE (Secondary electron) and BSE (Back scattered electron) images of the corroded surface of (a & b) 03Ti, (c) 1Ti and (d) 2Ti alloy respectively.

4. Conclusions

The present study is made on Fe-42%Ni super invar-based composition with a varying content of Y_2O_3/Ti ratio prepared by mechanical alloying and subsequently spark plasma sintered at 1000 °C for the microstructural characterization and mechanical properties. In this study, Ti amount was varied from 0.3, 1 and 2% while keeping other compositions (i.e., 42%Ni & 2%Y_2O_3) constant with a balanced Fe content. Increased Ti content especially 2% Ti addition in the base composition of Fe-Ni-Y_2O_3 is found to be very effective in achieving significant thermal stability with microstructural refinement in addition to the formation of nanoscale complex Y-Ti-O clusters, which subsequently resulted in better mechanical

properties, wear resistance and corrosion resistance. The significant outcome of the study is summarized as follows:

a) Ti addition in Fe-Ni alloys acts as a stabilizer to matrix grains, specifically when added with Y_2O_3. The Y_2O_3 decomposes into Y and O atoms during MA, and simultaneously dissolved into the metal matrix to form a supersaturated solid solution. The added Ti atoms combined with the dissolved Y and O, and subsequently reprecipitated as Y-Ti-O based nanoscale clusters uniformly distributed within the matrix. The XRD as well as TEM-SAED analysis confirmed the formation of nanosize $Y_2Ti_2O_7$ and TiO_2 dispersoids.

b) It was found that an increase in Ti content (0.3% to 2%) decreased the matrix grain size by ~40% (348 nm to 205 nm) and an increase in nanoindentation hardness by ~22% (4.2 GPa to 5.2 GPa). Hence, 2% Ti addition played a vital role in the formation of thermodynamically more stable $Y_2Ti_2O_7$ and TiO_2, which restricted the grain growth through Zenner pinning at high temperature.

c) EBSD-KAM analysis confirmed that the increase in the Ti addition increased dislocation density and microstrain within the material. Accumulation of higher dislocation density results in better dislocation strengthening and provides more support to shear strength and other mechanical properties.

d) It seems that effect of more Ti addition in Fe-Ni-Y_2O_3 has very low effect on corrosion properties. On the other hand, more amount of Ti addition (i.e., 2Ti alloy) is found to be very effective on increase in the wear resistance. The uniformly distributed nanoscale stable $Y_2Ti_2O_7$ and TiO_2 dispersoids in the metal matrix and adherent tribo-layered structure in the 2Ti alloy could prevent further wearing of the metal, and hence increased wear resistance subsequently.

Acknowledgment

Metallurgical and Materials Engineering Department and Institute Instrumentation Center, IIT Roorkee are highly acknowledged for granting all the facilities required to carry out the research work.

References

1) N. Singh, O. Parkash, D. Kumar, Phase evolution, mechanical and corrosion behavior of Fe(100-x) Ni(x) alloys synthesized by powder metallurgy, J. Phys. Chem. Solids, 114 (2018), pp. 8-20.
2) C.V. Prica, B.V. Neamtu, F. Popa, T.F. Marinca, N. Sechel, and I. Chicinas, Invar-type nanocrystalline compacts obtained by spark, plasma sintering from mechanically alloyed powders, J. Mater. Sci. 53 (2018) pp. 3735–3743.
3) S. Zheng, M. Sokoluk, G. Yao, I.D. Rosa, X. Li, Fe-Ni invar alloy reinforced by WC nanoparticles with high strength and low thermal expansions, SN Appl. Sci. 1 (2019), pp 172.
4) A. Arora, A. Kumar, and S. Mula, Effect of Y_2O_3 on mechanical and corrosion properties of Fe and Fe-Ni alloys prepared by mechanical alloying followed by spark plasma sintering, J. Mater. Eng. Perform., 30 (2021), pp. 1387–1397.
5) G.R. Odette, D.T. Hoelzer, Irradiation-tolerant nanostructured ferritic alloys: transforming helium from a liability to an asset, JOM, 62 (2010), pp. 84-92.
6) G.R. Odette, M.J. Alinger, B.D. Wirth, Recent developments in irradiation-resistant steels,
   Annu. Rev. Mater. Res, 38 (2008), pp. 471-503.
7) A. Kimura, R. Kasada, N. Iwata, H. Kishimoto, C.H. Zhang, J. Isselin, P. Dou, J.H. Lee, N. Muthukumar, T. Okuda, M. Inoue, S. Ukai, S. Ohnuki, T. Fujisawa, T.F. Abe, Development of Al added high-Cr ODS steels for fuel cladding of next generation nuclear systems, J. Nucl. Mater., 417 (2011), pp. 176-179.
8) L. Wang, Z. Bai, H. Shen, C. Wang, T. Liu, Creation of $Y_2Ti_2O_7$ nanoprecipitates to strengthen the Fe-14Cr-3Al-2W steels by adding Ti hydride and Y_2O_3 nanoparticles, J. Nucl. Mater., 488 (2017) pp. 319-327.
9) S. Ukai, S. Kato, T. Furukawa, S. Ohtsuka, High-temperature creep deformation in FeCrAl oxide dispersion strengthened alloy cladding, Mater. Sci. Eng. A, 794(2020), pp. 139863.
10) P.K. Kumar, N.V. Sai, A.G. Krishna, Effect of Y_2O_3 addition and cooling rate on mechanical properties of Fe-24Cr-20Ni-2Mn steels by powder metallurgy route, Compos. Commun.,10 (2018), pp. 116-121.

11) S. Shi, S. Cho, T. Goto, T. Kusunose, and T. Sekino, Combinative effects of Y_2O_3 and Ti on Al_2O_3 ceramics for optimizing mechanical and electrical properties, Ceram. Int., 15 (2018), pp. 18382-18388.

12) Z. Mu, H.R. Geng, M.M. Li, G.L. Nie, and J.F. Leng, Effects of Y_2O_3 on the property of copper-based contact materials, Compos. B. Eng., 52 (2013), pp. 51-55.

13) C. Lu, Z. Lu, R. Xie, Z. Li, C. Liu, and L. Wang, Effect of Y/Ti atomic ratio on microstructure of oxide dispersion strengthened alloys, Mater. Charact., 134 (2017), pp. 35-40.

14) M.J. Alinger, G.R. Odette, and D.T. Hoelzer, On the role of alloy composition and processing parameters in nanocluster formation and dispersion strengthening in nanostuctured ferritic alloys, Acta Mater., 57 (2) (2009), pp. 392-406.

15) H. Zhang, Y. Huang, H. Ning, C.A. Williams, A.J. London, K. Dawson, Z. Hong, M.J. Gorley, C.R. M. Grovenor, G.J. Tatlock, S.G. Roberts, M.J. Reece, H. Yan and P.S. Grant, Processing and microstructure characterisation of oxide dispersion strengthened Fe-14Cr-0.4Ti $0.25Y_2O_3$ ferritic steels fabricated by spark plasma sintering, J. Nucl. Mater., 464 (2015), pp. 61-68.

16) S. Peng, Z. Lu, L. Yu, Effects of Y_2O_3/Ti/Zr addition on microstructure and hardness of ODS-CoCrFeNi HEAs produced by mechanical alloying and spark plasma sintering, J. Alloys. Compd., 861 (2021), pp. 157940.

17) P. Perez, G. Salmi, A. Munoz, M.A. Monge, Influence of yttria additions on the oxidation behaviour of titanium prepared by powder metallurgy, Scr. Mater., 60 (11) (2009), pp. 1008-1011.

18) H. Kotan, K.A. Darling, R.O. Scattergood, C.C. Koch, Influence of Zr and nano-Y_2O_3 additions on thermal stability and improved hardness in mechanically alloyed Fe base ferritic alloys, J. Alloys Compd., 615 (2014), pp. 1013-1018.

19) O. Guillon, J. G. Julian, B. Dargatz, T. kessel, G. Schierning, J. Rather, M. Hermann, Field assisted sintering technology/spark plasma sintering: mechanisms, materials, and technology development, Adv. Eng. Mater. 16 (7) (2014), pp. 830-849.

20) Y. Cheng, Y. Qi, P. Hu, S. Zhou, G. Chen, J. An, K. Jin, W. Han, ZrB2-SiC-G Composite Prepared by Spark Plasma Sintering of In-Situ Synthesized ZrB2-SiC-C Composite Powders, J. Am. Ceram. Soc., 99 (16) (2016), pp. 2131–2137.

21) M. J. Paul, V.M.S. Muthaiah, S. Mula, Yrria -Reinforced Fe-Cr ferritic alloy, based nanocomposites for fusion reactor structural applications, Metall. Mater. Trans. A, 52 (2021), pp. 627-643.

22) C. Lu, Z. Lu, R. Xie, Z. Li, C. Liu, L. Wang, Effect of Y/Ti ratio on microstructure of dispersion oxide strengthened alloys, Mater. Charact., 134 (2017), pp. 35-40.

23) C. L. Chen, Sutrisna, Influence of alloying elements, in-situ dispersoids and fabrication on microstructure and properties of W-(Ta,V,Ti) ODS alloys, J. Alloys. Compd., 834 (2020), pp. 154952.

24) T. Roy, V. Shivam, K. Chattopadhyay, R. Manna, N.K. Mukhopadhyay, Microstructure evolution and mechanical properties of nano-yttria dispersed 316L austenitic stainless steel by mechanical alloying and sintering, Trans Indian Inst Met 74 (8) (2021), pp 2093–2104.

25) K.A. Darling, M. Kapoor, H. Kotan, B.C. Hornbuckle, S.D. Walck, G.B. Thompson, M.A. Tschopp, L.J. Kecskes, Structure and mechanical properties of Fe-Ni-Zr oxide-dispersion strengthened (ODS) alloys, J. Nucl. Mater., 467 (2015), 205-213.

26) C. Suryanarayana, Mechanical alloying and milling, Prog. Mater. Sci., 46 (2001), pp. 1-184.

27) M. Laurent-Brocq, F. Legendre, M.H. Mathon, A. Mascaro, S. Poissonnet, B. Radiguet, P. Pareige, M. Loyer, O. Leseigneur, Influence of ball-milling and annealing conditions on nanocluster characteristics in oxide dispersion strengthened steels, Acta Mater., 60(20) (2012), pp. 7150–7159.

28) I. Hilger, M. Tegel, M.J. Gorley, P.S. Grant, T. Weißgarber, B. Kieback, The structural changes of Y_2O_3 in ferritic ODS alloys during milling, J. Nucl. Mater., 447 (1–3) (2014), pp. 242–247.

29) P. Dou, Q. Ye, A. kimura, Crystal and metal/oxide interface structures of nanoparticles in 15Cr–2W–0.1Ti–4Al–0.6Hf–0.35Y_2O_3 ODS steel. J. Nucl. Mater., 553 (2020), pp. 152029.

30) L. B. Hong, and B. Fultz, Two-phase coexistence in Fe–Ni alloys synthesized by ball milling Journal of Applied Physics, Int. J. Appl. Phys., 79 (1996), pp. 3946.

31) Z. Li, R. Parsons, B. Zang, H. Kishimoto, T. Shoji, A. Kato, J. Karel, K. Suzuki, Dramatic grain refinement and magnetic softening induced by Ni addition in Fe based nanocrystalline soft magnetic alloys, Scr. Mater., 181 (2020), pp. 82-85.

32) S. Pasebani, I. Charit, Y.Q. Wu, D.P. Butt, J. I. Cole, Mechanical alloying of lanthana-bearing nanostructured ferritic steels, Acta Mater., 61(15) 2013, pp. 5605-5617.

33) B. Srinivasarao, K. Oh-ishi, T. Ohkubo, K. Hono, Bimodally grained high-strength Fe fabricated by mechanical alloying and spark plasma sintering, Acta Mater., 57(11) (2009), pp. 3277-3286.

34) C. Lu, Z. Lu, R. Xie, Z. Li, C. Liu, L. Wang, Effect of Y/Ti ratio on microstructure of dispersion oxide strengthened alloys, Mater. Charact., 134 (2017), pp. 35-40

35) S. Tekumalla, N. Bibhanshu, S. Suwas, M Gupta, Superior ductility in magnesium alloy-based nanocomposites: the crucial role of texture induced by nanoparticles, J. Mater. Sci., 54 (2019), pp. 8711–8718.

36) G. E. Dieter, Mechanical metallurgy, 3rd ed., McGraw Hill Education (India) Edition, 2013.

37) V. Raghavan, Physical metallurgy, 2nd ed., Principles and Practice, 2014.

38) S. Peng, Z. Lu, L. Yu, Effects of Y_2O_3/Ti/Zr addition on microstructure and hardness of ODS-CoCrFeNi HEAs produced by mechanical alloying and spark plasma sintering, J. Alloy. Compd. 861 (2021), pp. 157940.

39) A. Zunger, L.G. Wang, G.L.W. Hart, M. Sanati, Obtaining Ising-like expansions for binary alloys from first principles, Model. Simul. Mater. Sci. Eng., 10 (2002), pp. 685–706.

40) J.Y. Hong, Y.T. Shin, H.W. Lee, Characterization of corrosion resistance in a ferritic stainless steel stabilized with Ti addition, Int. J. Electrochem. Sci., (9) 2014, pp. 7325 – 7334.

41) E.A. Lizlovs, A.P. Bond, The effect of low-temperature aging on corrosion resistance of 18Cr-2Mo titanium-stabilized ferritic stainless steel, J. Electrochem Soc., 122 (1975), pp. 5.

42) J.E. Garay, U.A. Tamburini, Z. A. Munir, Enhanced growth of intermetallic phases in the Ni–Ti system by current effects, Acta Mater., 51(15) (2003), pp. 4487-4495.

43) P. Salvetr, T.F. Kubatik, D. Pignol, P. Novak, Fabrication of Ni-Ti alloy by self-propagating high-temperature synthesis and spark plasma sintering technique, Metall. Mater. Trans. B, 48 (2017), pp. 772–778.

44) G. Suprobo1, A. A. Ammar, N Park, E. R. Baek, S. Kim, Thermal decomposition of massive phase to fine lamellar α/β in Ti–6Al–4V additively manufactured alloy by directed energy deposition, Met. Mater. Int., 25 (2019), pp. 1428–1435.

45) G.X. Qiu, D.P. Zhan, C.S. Li, M. Qi, Z.H. Jiang, H.S. Zhang, Effects of Y and Ti addition on microstructure stability and tensile properties of reduced activation ferritic/martensitic steel, Nucl. Eng. Technol. 51 (2019) pp. 1365-1372.

46) Y. Geng, X. Li, H. Zhou, Y. Zhang, Y. Jia, B. Tian, Y. Liu, A. A. V, X. Zhang, K. Song, G. Wang, L. Li, J. Hou, Effect of Ti addition on microstructure evolution and

precipitation in Cu-Co-Si alloy during hot deformation, J. Alloys Compd. 821 (2020) pp. 153518.

47) S. Dehgahi, M. Sanjari, M.H. Ghoncheh, B.S. Amirkhiz, M. Mohammadi, Concurrent improvement of strength and ductility in heat-treated C300 maraging steels produced by laser powder bed fusion technique, Addit. Manuf. 39 (2021), pp. 101847.

48) Y. Geng, Y. Ban, B. Wang, X. Li, K. Song, Y. Zhang, Y. Jia, B. Tian, Y. Liu, A.A. Volinsky, A review of microstructure and texture evolution with nanoscale precipitates for copper alloys, J. Mater. Res. Technol., 9(5) (2020), pp. 11918-11934.

49) F. He, Z. Wang, B. Han, Q. Wu, D. Chen, J. Li, J. Wang, C.T. Liu, J.J. Kai, Solid solubility, precipitates, and stacking fault energy of microalloyed CoCrFeNi high entropy alloys, J. Alloys Compd. 769 (2018), pp. 490-502.

50) Y. Geng, Y. Ban, X. Li, Y. Zhang, Y. Jia, B. Tian, M. Zhou, Y.Liu, A.A. Volinsky, K. Song, S. Tang, Excellent mechanical properties and high electrical conductivity of Cu-Co-Si-Ti alloy due to multiple strengthening, Mater. Sci. Eng. A, 821 (2021), pp. 141639.

51) Y. Han, J. Shi, L. Xu, W.Q. Cao, and H. Dong, Effects of Ti addition and reheating quenching on grain refinement and mechanical properties in low carbon medium manganese martensitic steel, Mater. Des., 34 (2012), pp. 427–434.

52) H. Besharatloo, M. de Nicolas, J.J. Roa, M. Dios, A. Mateo, B. Ferrari, E. Gordo, L. Llanes, Assessment of mechanical properties at microstructural length scale of Ti(C, N)–FeNi ceramic-metal composites by means of massive nanoindentation and statistical analysis, Ceram. Int., 45(16) (2019), pp. 20202–20210.

53) A. Jain, B. Basu, B.V.M. Kumar, Harshavardhan, J. Sarkar, Grain size–wear rate relationship for titanium in liquid nitrogen environment, Acta Mater., 58(7) 2010, pp. 2313–2323.

54) Z.N. Farhat, Y. Ding, D.O. Northwood, A.T. Alpas, Effect of grain size on friction and wear of nanocrystalline aluminium, Mater. Sci. Eng. A, 206(2) (1996), pp. 302-313.

55) H. Zengin, M. E. Turan, Y. Turen, H. Ahlatci, Y. Sun, Influence of titanium addition on wear properties of AM60 magnesium alloy, IJMME, 10(61) (2016), pp. 767-771.

56) R.L. Deuis, C. Subramanian, and J.M. Yellup, Abrasive Wear of Aluminium Composites—A Review, Wear, 201 (1996), pp. 132–144.

57) Y. Mazaheri, F. Karimzadeh, M.H. Enayati, Tribological behavior of A356/Al2O3 surface nanocomposite prepared by friction stir processing, Metall. Mater. Trans. A, 45(4) (2013), pp. 2250–2259.

58) M.V.N.V. Satyanarayana, A. Kumar, Microstructure evolution, mechanical and corrosion behavior of cryogenic friction stir processed AA2014 alloy, Adv. Eng. Mater, (2021), 2100301.

59) W. Xu, J. Liu, H. Zhu, Pitting corrosion of friction stir welded aluminum alloy thick plate in alkaline chloride solution, Corros. Sci.,55(8) (2010), pp. 2918-2923.

60) S. Candan, M. Unal, E. Koc, Y. Turen, and E. Candan, Effects of titanium addition on mechanical and corrosion behaviours of AZ91 magnesium alloy, J. Alloys compd., 509(5) (2011), pp. 1958–1963.

61) V. M. S. Muthaiah, S. Mula, Influence of Cr and Y addition on microstructure, mechanical properties, and corrosion resistance of SPSed Fe-Based Alloys, Metall. Mater. Trans. A, 49 (2018), pp. 990-1005.

62) H. Zhao, T. Liu, Z. Bai, L. Wang, W. Gao, L Zhang, Corrosion behavior of 14Cr ODS steel in supercritical water: The influence of substituting Y_2O_3 with $Y_2Ti_2O_7$ nanoparticles, Corros. Sci., 163 (2020), pp. 108272.

63) P. Ampornrat and G.S. Was, Oxidation of ferritic-martensitic alloys T91, HCM12A and HT-9 in supercritical water, J. Nucl. Mater., 371(1-3) (2007), pp. 1-17.

CRediT authorship contribution statement

Arpan Arora: Formal testing & analysis, Data curation, Writing - original draft. **Suhrit Mula**: Supervision, Conceptualization, Writing-Reviewing and Editing

Declaration of Competing Interest

☒ The authors declare that they have no known competing financial interests or personal relationships that could have appeared to influence the work reported in this paper.

☐The authors declare the following financial interests/personal relationships which may be considered as potential competing interests:

Highlights

- Role of Ti/Y_2O_3 in Fe-42%Ni invar studied on phase evolution after mechanical alloying + SPS.
- XRD phase analysis and TEM-SAED study confirmed evolution of Y-Ti-O complex dispersoid.
- Superior thermal stability of 2%Ti alloy is confirmed by EBSD resulting an equiaxed sub-micron size (205nm) grains.
- Uniformly dispersed nanoscale Y-Ti-O clusters in 2%Ti alloy resulted better hardness, wear & corrosion resistance.
- Orowan strengthening & Zenner pinning played pivotal roles to yield high thermal stability & ultrafine structure.